



1 **Blowing snow contributions to the Arctic snow-on-sea ice
2 budget using ICESat-2 observations**

3

4 Joseph Robinson¹, Lyatt Jaeglé¹, Stephen P. Palm^{2,3}, Glen E. Liston⁴

5

6 ¹ Department of Atmospheric and Climate Science, University of Washington, Seattle, WA, USA

7 ² Science Systems and Applications, Lanham, MD, USA

8 ³ NASA Goddard Space Flight Center, Greenbelt, MD, USA

9 ⁴ Cooperative Institute for Research in the Atmosphere (CIRA), Colorado State University, Fort Collins, CO, USA

10

11 *Correspondence to:* Joseph Robinson (jrobin15@uw.edu)

12

13

14

15

16

17

18

19

20

21

22

23

24

25

26

27

28

29

30

31

32

33

34

35

36

37

38

39

40

41

42

43

44

45

46



47 **Abstract**

48

49 Blowing snow modulates the evolution of snow over Arctic sea ice through redistribution and
50 sublimation. Here, we present the first multi-year pan-Arctic observational estimates of blowing
51 snow occurrence, properties, and associated fluxes based on NASA Ice, Cloud and land
52 Elevation Satellite 2 (ICESat-2) satellite observations for five cold seasons (November through
53 April 2018–2023). On average, ICESat-2 detects blowing snow 19% of the time over sea ice,
54 with localized frequencies reaching up to 35% in the Central Arctic, where blowing snow heights
55 (optical depths) reach 150 m (0.20). We find that blowing snow occurrence shows strong
56 interannual variability related to large-scale climate variability, particularly the Arctic Oscillation
57 (AO). During positive AO phases, blowing snow occurrence increases substantially, with up to a
58 two-fold increase in the Central Arctic. Blowing snow occurrence, height, and optical depth all
59 exhibit a strong dependence on wind speed, increasing by more than five-fold between 4 and 15
60 m s^{-1} . ICESat-2 blowing snow sublimation estimates average 1.63 cm snow-water-equivalent
61 (SWE) per cold season, thus removing 14% of pan-Arctic snowfall. In the Central Arctic, the
62 offset is 18–24%. These values are consistent with simulations from the high-resolution
63 SnowModel-LG (1.66 cm SWE) and a simpler, threshold-based model (2.07 cm SWE).
64 Interannual variability in snowfall and sublimation can be 1–2 cm SWE, though not always in
65 phase, resulting in snowfall removals that range from 9% to 20%. Critically, these findings
66 provide satellite-based constraints on blowing snow processes over sea ice and underscore the
67 importance of blowing snow sublimation in the Arctic snow budget.

68

69 **1 Introduction**

70

71 Snow cover on sea ice is a fundamental component of the Arctic climate system, influencing
72 surface albedo, insulating the ocean from the atmosphere, and modulating the exchange of heat
73 and moisture across the ocean-ice-atmosphere interface (Merkouriadi, Cheng, et al., 2017;
74 Merkouriadi, Gallet, et al., 2017; Sturm et al., 2002; Webster et al., 2018). Its presence impacts
75 not only the local energy balance but also broader climate feedbacks that affect both high- and
76 mid-latitudes. As the Arctic undergoes rapid environmental change, including thinning sea ice
77 (Kwok & Untersteiner, 2011; Stroeve & Notz, 2018), shifting precipitation patterns (Bintanja,
78 2018; Bintanja & Andry, 2017; McCrystall et al., 2021), and increasing temperatures (Rantanen
79 et al., 2022), the need to accurately characterize the spatial and temporal variability of snow on
80 sea ice has become increasingly urgent. Understanding how the snowpack and its properties
81 evolve across a range of spatial and temporal scales and in response to dynamic atmospheric
82 processes is essential for improving predictions of sea ice behavior, refining climate model
83 simulations, and assessing implications for Arctic ecosystems, human activities, and global
84 climate.

85

86 While the snowpack on sea ice generally follows a seasonal cycle of winter accumulation and
87 summer melt, shorter-term processes can alter characteristics and accumulation rates. One such
88 process is blowing snow, which occurs when strong winds lift snow away from the surface.
89 Numerous studies spanning several decades have underscored the role of blowing snow in
90 modulating sea and land ice mass balance (Déry & Yau, 2002; Gallée et al., 2001; Palm et al.,
91 2017), altering radiative properties in polar regions (Lesins et al., 2009; Y. Yang et al., 2014),
92 impacting chemical processes in the polar troposphere (Frey et al., 2020; Gong et al., 2023;



93 Huang et al., 2020; Huang & Jaeglé, 2017; Krnavek et al., 2012; X. Yang et al., 2008), and
94 complicating the interpretation of physical and chemical ice core records (King et al., 2004;
95 Rhodes et al., 2017). Yet, capturing the full spatial and temporal variability of blowing snow
96 remains challenging due to the limited availability of sustained, regionally comprehensive
97 observations (Déry & Yau, 2001; Mann et al., 2000; Nishimura & Nemoto, 2005).

98

99 When lifted into the air, blowing snow particles are exposed to conditions that can promote their
100 sublimation, making blowing snow sublimation a significant pathway for both snow removal and
101 a source of atmospheric moisture. While sublimation can occur directly at the snow surface, it is
102 far more efficient when particles are suspended aloft, where their full surface area interacts with
103 the ambient air (Liston & Sturm, 2004; Schmidt, 1982). Model-based assessments suggest a
104 substantial role for this process in the Arctic hydrological cycle: J. Yang et al. (2010) estimated
105 that over 27% of winter snowfall poleward of 70°N may be lost to blowing snow sublimation.
106 However, other modeling studies (e.g., Chung et al., 2011; Déry & Yau, 2002) have reported
107 much lower estimates (6–7%), underscoring the considerable uncertainty that still surrounds
108 blowing snow related processes. Narrowing these uncertainties and understanding the
109 implications of sublimation-driven snow loss over sea ice remains a pressing scientific challenge.

110

111 The time evolution of snow-water-equivalent (SWE) depth can be described by the mass balance
112 equation:

113

114
$$\frac{dSWE}{dt} = \frac{1}{\rho_w} [P - (M + Q_{ss} + Q_{bs}) + Q_t] \quad (1)$$

115

116 where ρ_w is the density of water, and the terms represent inputs from precipitation (P ; $\text{kg m}^{-2} \text{s}^{-1}$)
117 and losses via melt (M , $\text{kg m}^{-2} \text{s}^{-1}$) and sublimation ($\text{kg m}^{-2} \text{s}^{-1}$), either from a static, non-blown
118 snow surface (Q_{ss}) or via blowing snow (Q_{bs}). Erosion and deposition by blowing snow transport
119 (Q_t , $\text{kg m}^{-2} \text{s}^{-1}$) can also play a role in shaping the local snowpack. While Eq. 1 represents key
120 drivers of snowpack evolution, other processes, such as ice dynamics (e.g., creation and
121 destruction of parcels through ice motion, divergence, and convergence), may also play
122 important roles.

123

124 Efforts to quantify the influence of blowing snow on SWE often rely on empirical
125 parameterizations of snow transport and sublimation derived from sparse observations. These
126 approaches typically use meteorological inputs such as windspeed, air temperature, and snow age
127 to estimate thresholds for blowing snow initiation and subsequent sublimation (e.g., Gallée et al.,
128 2001, 2013; Lenaerts et al., 2010, 2012). In the Northern Hemisphere, model development has
129 primarily focused on continental snowpacks (Déry & Yau, 2001, 2002; Pomeroy et al., 1997; J.
130 Yang & Yau, 2007), where snow redistribution is critical to understand human-relevant
131 hydrology and impacts to infrastructure. Although several studies have extended these
132 approaches to sea ice environments (Chung et al., 2011; Déry & Tremblay, 2004; Lecomte et al.,
133 2015; Liston et al., 2018, 2020; J. Yang et al., 2010), there remains a lack of direct, observation-
134 based constraints on pan-Arctic blowing snow processes over sea ice.

135

136 Spaceborne lidars offer a powerful means to address observational gaps and assess the
137 occurrence and impacts of blowing snow across large spatial and temporal domains. Palm et al.
138 (2011, 2017, 2018) developed a detection algorithm for the Cloud-Aerosol Lidar with



139 Orthogonal Polarization (CALIOP) aboard NASA's CALIPSO satellite (Winker et al., 2009),
140 demonstrating that lidar backscatter measurements can be used to quantify key blowing snow
141 characteristics over Antarctica, including frequency of occurrence, height, optical depth, and
142 associated transport and sublimation fluxes. Building on this approach, a similar algorithm was
143 later adapted for the NASA Ice, Cloud, and land Elevation Satellite-2 (ICESat-2; Markus et al.,
144 2017) by Palm et al. (2021) and Herzfeld et al. (2021). Both algorithms were tailored to detect
145 blowing snow over the Antarctic continent. More recently, Robinson et al. (2025) optimized the
146 ICESat-2 blowing snow detection algorithm for application over Arctic sea ice, where more
147 frequent low-level cloud cover (Shupe et al., 2011; Zhang et al., 2019) increases the likelihood of
148 both false positives (i.e., clouds misidentified as blowing snow) and false negatives (i.e., blowing
149 snow misclassified as clear air) in lidar retrievals. Robinson et al. (2025) demonstrated that
150 retrieval errors caused by cloud interference can be effectively corrected, enabling the
151 development of a space-based blowing snow detection product specifically adapted for Arctic
152 sea ice.

153
154 In this study, our goal is to examine blowing snow occurrence and properties inferred from
155 ICESat-2 over Arctic sea ice across five cold seasons (defined as November through April)
156 between 2018 to 2023. We use ICESat-2 observations to infer blowing snow sublimation and its
157 role in the snow-on-sea ice budget. We compare the ICESat-2 observations to blowing snow
158 simulations from two models of varying complexity: a parameterization based on the PIEKTUK
159 blowing snow model (DY2001; Déry & Yau, 1999, 2001; J. Yang & Yau, 2007) and the state-of-
160 the-art Lagrangian snow-evolution model SnowModel-LG (Liston et al., 2020).
161

162 In Section 2 we provide details on the ICESat-2 blowing snow retrievals and inferred blowing
163 snow properties, SnowModel-LG predictions, and the DY2001 blowing snow sublimation
164 formulation. In Section 3 we present the ICESat-2 multi-year blowing snow occurrence
165 frequency and properties, examining key drivers of their spatiotemporal distribution. The role of
166 blowing snow in the snow-on-sea-ice budget is examined in Section 4 and conclusions are
167 presented in Section 5.
168

169 **2 Datasets and Methods**

170 **2.1 Satellite blowing snow retrievals from ICESat-2**

171 ICESat-2 was launched in 2018 in a precessing orbit with an altitude of ~ 500 km and inclination
172 of 92° , which allows for measurements up to 88° N latitude with a 91-day orbital repeat cycle
173 (Markus et al., 2017). ICESat-2 carries the Advanced Topographic Laser Altimeter System
174 (ATLAS), which is a single wavelength (532 nm), high repetition rate (10 kHz) lidar system with
175 photon counting detectors (Markus et al., 2017; Neumann et al., 2019). Each ATLAS laser pulse
176 is split into 3 simultaneous beam pairs (one strong and one weak beam per pair) by a diffractive
177 optical element. The 3 beam pairs are separated by about 3 km across track. Atmospheric
178 backscatter is obtained by ATLAS using only the three strong beams, spanning from the surface
179 to an altitude of 14 km, with an along-track resolution of approximately 280 m and a vertical
180 resolution of 30 m. Each 280 m ICESat-2 atmospheric profile represents the aggregate of 400
181 individual ATLAS laser shots (Palm et al., 2021). In this study we use ICESat-2 strong beam 1
182 observations from version 6 of the ATLAS/ICESat-2 Level 3A (ATL09) calibrated backscatter
183 profile product (Palm et al., 2023).
184



185

186 The algorithm used to detect blowing snow in ATLAS backscatter profiles is adapted from the
187 CALIOP approach (Palm et al., 2011) and further detailed in Palm et al. (2021; 2022). When a
188 surface return is identified and the 10 m wind speed from NASA's GEOS-5 FP-IT analysis
189 exceeds 4 m s^{-1} , the algorithm compares the near-surface atmospheric backscatter to the expected
190 molecular (Rayleigh) signal. If the observed signal exceeds a fixed multiple of the molecular
191 scattering, the algorithm steps upward through each vertical bin until the backscatter drops below
192 an adaptive threshold (typically $\sim 2 \times 10^{-5} \text{ m}^{-1} \text{ sr}^{-1}$). To be flagged as blowing snow, the detected
193 feature must touch the ground and be shallower than 500 m. Retrievals deeper than 500m are
194 classified as diamond dust, which can stretch for a km or more vertically and frequently reaches
195 the ground (Intrieri & Shupe, 2004). Further, we use the version of the blowing snow algorithm
196 described in Robinson et al. (2025) which includes modifications to help alleviate several
197 challenges unique to the Arctic. These modifications serve to 1) minimize the misidentification
198 of low clouds as blowing snow and 2) correct for the attenuation due to transmissive clouds.

199

200 Once blowing snow is retrieved, its properties (geometric and optical depths) are logged. Optical
201 depth (OD) is estimated as the sum of the backscatter within the blowing snow retrieval
202 multiplied by the product of the bin depth (30 m) and the extinction to backscatter (lidar) ratio. A
203 lidar ratio of 25 sr is used, which is a typical value for ice crystals in cirrus clouds (Chen et al.,
204 2002; Josset et al., 2012). To infer blowing snow particle number density, transport flux, and
205 sublimation flux from the observed ICESat-2 backscatter we follow the same approach as
206 described in Palm et al. (2017) and Robinson et al. (2025), which relies on meteorological fields
207 (10 m wind speed, 2 m temperature, and 2 m relative humidity over ice) from the NASA GEOS-
208 5 FP-IT analysis (run at 0.5° latitude $\times 0.625^\circ$ longitude; Lucchesi et al., 2015) as well as
209 assumptions about blowing snow particle size. As in Robinson et al. (2025) we use the
210 formulation $r(z) = 5.05 \times 10^{-5} z^{-0.085}$ to estimate the particle radius (r , meters) as a function of
211 altitude (z , meters). This fit was constrained by observations of blowing snow particle sizes
212 during the 2019-2020 Multidisciplinary drifting Observatory for the Study of Arctic Climate
213 (MOSAiC) campaign.

214

215 To improve signal-to-noise in sunlit conditions, we apply along-track averaging to the ICESat-2
216 observations when the solar elevation angle exceeds -7° , a threshold beyond which background
217 solar photons begin to significantly degrade sensitivity. Under these conditions, which affect late
218 February through April (Fig. S1), increased solar background can reduce the detectability of low-
219 backscatter features such as blowing snow. To mitigate this, we average the native 25 Hz (280
220 m) profiles to 1 Hz (~ 7 km) resolution, effectively reducing solar background noise and
221 enhancing the reliability of blowing snow retrievals. While this approach lowers spatial
222 resolution, it reduces false positive detections and provides a more robust estimate of blowing
223 snow properties under marginal lighting conditions without introducing significant biases in
224 seasonal statistics.

225

226 **2.2 Blowing snow model simulations from SnowModel-LG**

227

228 SnowModel-LG is a physics-based snow-on-sea ice model forced by atmospheric inputs of air
229 temperature, RH, winds, and precipitation by the NASA Modern-Era Retrospective analysis for
230 Research and Applications, version 2 (MERRA-2; Gelaro et al., 2017) as well as sea ice inputs



231 of concentration and parcel motion (Tschudi et al., 2019, 2020). At each 3-hour timestep,
232 SnowModel-LG performs mass-budget calculations (e.g., Eq. 1) where SWE depth evolution is
233 accounted for by snow gains, losses, and sea ice dynamics (Liston et al., 2020).

234
235 The MicroMet module (Liston & Elder, 2006) is used to time average (1-hourly to 3-hourly) and
236 distribute the MERRA-2 fields (0.5° latitude $\times 0.625^\circ$ longitude) to the sea ice parcels. As part of
237 this procedure, the MERRA-2 water equivalent precipitation is bias corrected (as described in
238 section 2.5 and Table 1 of (Liston et al., 2020) and partitioned into snowfall and rainfall based on
239 environmental conditions (Dai, 2008).

240
241 Blowing snow in SnowModel-LG is accounted for by SnowTran-3D (Liston et al., 2007, 2018;
242 Liston & Sturm, 1998). The snow threshold friction velocity, u_{*t} , is calculated as a function of
243 snow density, ρ_s , which is related to snow strength and hardness. Snow density evolution
244 includes the history of temperature, precipitation, and wind-transport. When the friction velocity
245 exceeds the threshold value, snow begins to be lifted off the surface, first into the saltation layer
246 (several cm thick) and then into the turbulent suspension layer (several m thick). The vertical
247 mass concentration in the blowing snow profile is estimated following Liston & Sturm (1998)
248 and is combined with the environmental conditions to calculate transport and sublimation fluxes.
249 Mass transport is related to the windspeed and vertical mass concentration. SnowModel-LG's
250 blowing snow sublimation is calculated as a function of several factors, including the vertical
251 mass concentration, temperature-dependent humidity gradients between the snow particles and
252 the atmosphere, conductive and advective energy- and moisture-transfer mechanisms, particle
253 size, and solar radiation. The SnowModel-LG blowing snow transport and sublimation fluxes
254 represent column integrated values in units of $\text{kg m}^{-1} \text{s}^{-1}$ and cm SWE d^{-1} , respectively.
255 SnowModel-LG variables are output as 3-hourly values on an EASE grid with a resolution of 25
256 km.

257
258 **2.3 Blowing snow sublimation estimates from DY2001**

259
260 We also include estimates of the bulk blowing snow sublimation rate (Q_{bs} in Eq. 1) using the
261 approach described by Déry & Yau (1999, 2001) and subsequently J. Yang & Yau (2007).
262 Throughout the analysis we refer to this approach as DY2001. We chose to include it because it
263 is computationally efficient and has been widely applied in studies of blowing snow aerosol
264 production over sea ice (e.g., Gong et al., 2023; Frey et al., 2020; Huang et al., 2020; Huang &
265 Jaeglé, 2017; X. Yang et al., 2008, 2019). Sublimation depends on several factors including
266 surface windspeed, temperature, and humidity deficit.

267
268 Following X. Yang et al. (2008), sublimation is scaled by snow age A' which accounts for the
269 reduced ease of wind lofting as snow ages. For a full description of the sublimation calculation
270 used here, we refer the reader to section 2.1.1 of X. Yang et al. (2008). In our calculations, we
271 adopt a representative mean snow age of 3 days over Arctic sea ice (Huang & Jaeglé, 2017).

272
273 A key factor controlling blowing snow occurrence in DY2001 is the threshold windspeed, which
274 follows Li & Pomeroy (1997a). The threshold windspeed ($U_t = 6.975 + 0.0033/[T_{2m} + 27.27]/^2$) is
275 estimated from the 2 m surface air temperature (T_{2m}) and has a minimum value of $\sim 7 \text{ m s}^{-1}$ at an
276 air temperature of -27°C . At both higher and lower temperatures, the threshold wind speed will



277 be larger (maximizing at $\sim 10 \text{ m s}^{-1}$ for temperatures near 0°C). We estimate the DY2001
278 threshold windspeed and blowing snow sublimation using the same meteorology (10 m
279 windspeed, 2 m temperature, and 2 m RH_{ice}) used to derive the ICESat-2 sublimation.
280

281 **2.4 ICESat-2 and model gridding procedure**

282

283 We aggregate the ICESat-2 observations to a National Snow and Ice Data Center (NSIDC)
284 Equal-Area Scalable Earth (EASE) grid (Brodzik & Knowles, 2002) with a horizontal resolution
285 of 100 km. This resolution balances spatial detail with observational coverage, ensuring
286 sufficient ICESat-2 sampling within each grid cell while minimizing noise that would arise at
287 finer resolutions due to the narrow swath of the lidar. Temporal resolution is determined by the
288 duration of the binning period, allowing flexibility to examine daily, seasonal, or multi-year
289 patterns.
290

291

292 Within each 100 km grid cell, the blowing snow occurrence for a specified time window is
293 computed as the number of profiles with a blowing snow detection divided by the total number
294 of valid profiles. A valid profile is defined as one where the surface return is clearly detected,
295 which excludes profiles with optically thick cloud cover (optical depth > 3), where surface
296 detection is unreliable or is not achieved. For blowing snow properties such as geometric and
297 optical depths, only blowing snow retrievals are gridded.
298

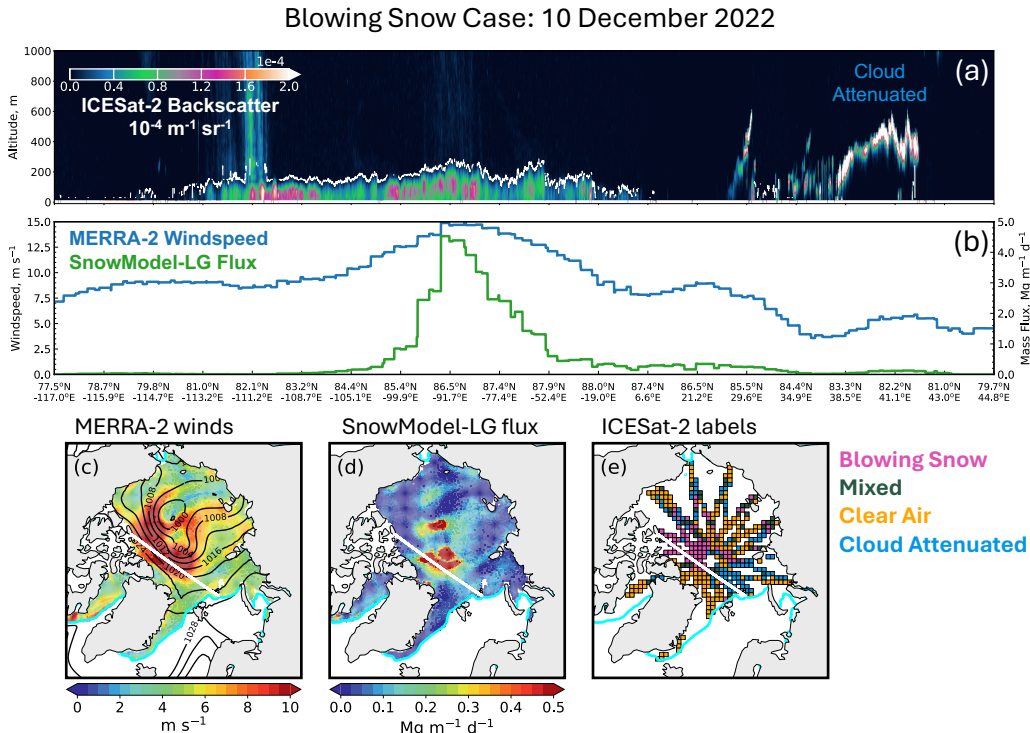
299

300 For comparison with model estimates, we extract values from the SnowModel-LG fields (25 km
301 resolution) by sampling the nearest-neighbor grid point to each valid ICESat-2 profile location.
302 These sampled values are then binned to the same 100 km EASE grid alongside the ICESat-2
303 data. We apply the same procedure to the DY2001 estimates: values are first computed at the
304 location of each valid ICESat-2 profile, and the resulting fields are aggregated onto the 100 km
305 grid for direct comparison with both ICESat-2 observations and SnowModel-LG outputs.
306

307 **2.5 December 2022 example of observed and predicted blowing snow**

308

309 Figure 1 highlights a blowing snow storm which occurred over the Central Arctic in December
310 2022. During an orbit which transited from Svalbard towards the Canadian Arctic Archipelago,
311 ICESat-2 retrieved blowing snow for roughly 1,200 km along track, with depths up to 250 m and
312 observed backscatter exceeding $1.50 \times 10^{-4} \text{ m}^{-1} \text{ sr}^{-1}$ (Fig. 1a). In this region, MERRA-2
313 windspeeds ranged from 7.5 to 15 m s^{-1} (blue line, Fig. 1b) and SnowModel-LG predicted
314 intense blowing snow, with mass fluxes peaking at $4 \text{ Mg m}^{-1} \text{ d}^{-1}$ (green line, Fig. 1b). The
315 strongest ICESat-2 observed and SnowModel-LG predicted blowing snow occurred coincident
316 with the strongest winds (middle of Fig. 1a,b). While ICESat-2 did retrieve blowing snow to the
317 west of this maximum (left side, Fig. 1a) coincident with windspeeds $> 8 \text{ m s}^{-1}$, SnowModel-LG
318 predicted only minimal blowing snow mass transport.
319



318
 319

320 **Figure 1.** Case study of a blowing snow event in the Central Arctic on 10 December 2022. (a) ICESat-2 backscatter
 321 (shading, units $\text{m}^{-1} \text{sr}^{-1}$) along an orbit from the Canadian Arctic Archipelago towards north of Svalbard. The white
 322 line indicates the top of the blowing snow layer. (b) MERRA-2 windspeed (blue line, units m s^{-1}) and SnowModel-
 323 LG blowing snow mass transport (green line, units $\text{Mg m}^{-1} \text{d}^{-1}$) along the ICESat-2 orbit shown in panel a. (c) Spatial
 324 distribution of MERRA-2 windspeed (shading, units m s^{-1}) with sea-level pressure contours (black, 4 hPa intervals).
 325 (d) Spatial distribution of SnowModel-LG blowing snow mass transport (shading, units $\text{Mg m}^{-1} \text{d}^{-1}$). (e) ICESat-2
 326 classifications at 100 km resolution: blowing snow (magenta), mixed (green), clear air (orange), or cloud attenuated
 327 (blue) as described in Section 2.5. In panels c-e, the cyan line marks the 15% sea ice contour, while the white line
 328 shows the track of ICESat-2 from panel a.

329

330 Winds in excess of 8 m s^{-1} covered much of the Central Arctic and coincided with tight sea-level
 331 pressure (SLP) gradients stretching from the Beaufort to Lincoln Sea (Fig. 1c). SnowModel-LG
 332 predicted blowing snow mass transport $> 0.20 \text{ Mg m}^{-1} \text{d}^{-1}$ over an area of $750,000 \text{ km}^2$ (Fig. 1d),
 333 which is slightly larger in size than the state of Texas. Given a total Central Arctic area of
 334 roughly 3.2 million km^2 , this storm impacted about a quarter of the basin.

335

336 To examine the spatial distribution of ICESat-2 profiles, we first gridded the ICESat-2 orbits to
 337 the 100 km grid (Section 2.4) and then assigned each grid cell to one of four categories: blowing
 338 snow, mixed, clear air, or cloud attenuated. If more than 70% of all profiles were attenuated due
 339 to clouds, the grid cell was labeled as cloud attenuated. We assigned the other three categories
 340 based on the occurrence of blowing snow: blowing snow if more than 50% of profiles were
 341 blowing snow, mixed if 15-50% of profiles were blowing snow, and clear air if less than 15% of
 342 profiles were blowing snow. ICESat-2 grid cells in the western Central Arctic were consistently

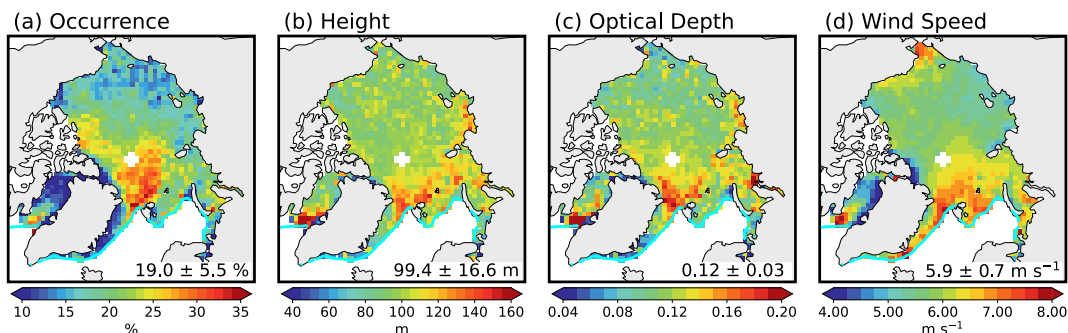


343 classified as blowing snow (magenta colors, Fig. 1e), coinciding with the strongest winds and the
344 highest SnowModel-LG predicted transport. The total area of ICESat-2 grid cells labeled as
345 blowing snow was 740,000 km², closely matching the SnowModel-LG predictions and
346 confirming that the blowing snow was synoptic in scale, covering much of the Central Arctic.
347

348 **3 Blowing snow occurrence frequency and properties from ICESat-2** 349 **3.1 Spatiotemporal variability and drivers of blowing snow occurrence**

350 Figure 2 shows the mean multi-year blowing snow occurrence and properties derived from the
351 ICESat-2 observations for November through April 2018-2023. To generate the average maps,
352 we grid each cold season independently (following Section 2.4) and then average the five cold
353 seasons together. We found a significant fraction of the central Arctic experiences blowing snow
354 frequencies > 25%, with maxima of near 35% in the Fram Strait region (Fig. 2a). This is
355 consistent with several previous studies which showed these regions have consistent influence (>
356 15% of the time) from storms entering the Arctic (e.g., Clancy et al., 2022; Valkonen et al.,
357 2021). This is also evident in the spatial distribution of MERRA-2 windspeeds (Fig. 2d), where
358 the region of high blowing snow occurrence frequency is collocated with average windspeeds >
359 6.5 m s⁻¹.
360

361



362
363

364 **Figure 2.** Mean ICESat-2 blowing snow properties during the cold season (November-April, 2018-2023): (a)
365 occurrence frequency, (b) blowing snow geometrical depth, (c) optical depth, and (d) MERRA-2 10 m wind speed.
366 The cyan line marks the 15% sea ice contour. Numbers in the bottom right of each panel correspond to the mean and
367 standard deviation for values over sea ice.

368

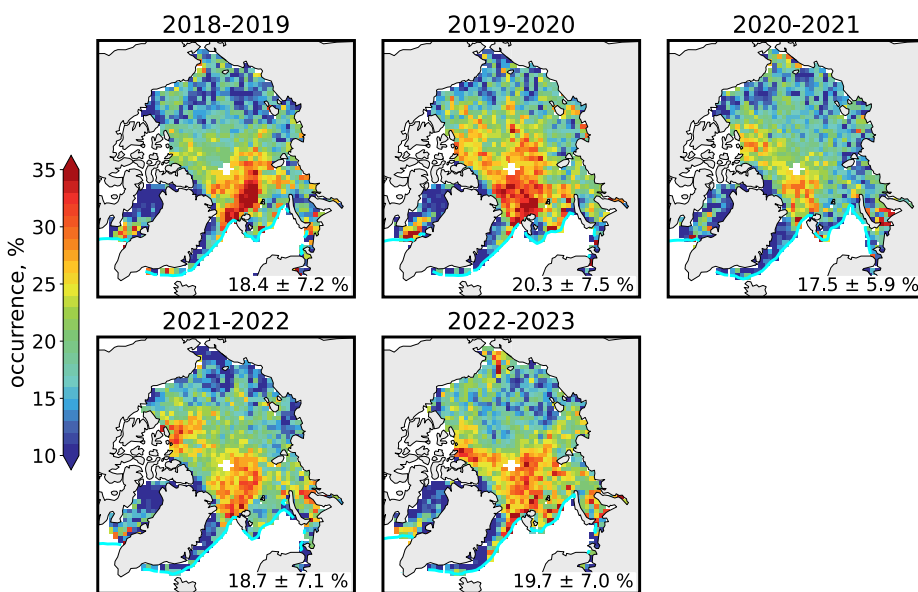
369 The ICESat-2 occurrence frequency does not include shallow (< 30 m thick) blowing snow
370 layers, since these cannot be reliably detected at the vertical resolution of the atmospheric
371 backscatter profiles. In addition, ICESat-2 cannot sample conditions where optically thick clouds
372 prevent the surface from being detected. Regions of the Kara, Barents, and Greenland Seas are
373 particularly susceptible to this under sampling, where the ICESat-2 cloud attenuated occurrence
374 (% of all profiles where the surface cannot be detected) can exceed 50% across much of the cold
375 season (Fig. S2).
376

377

378 The multi-year cold season ICESat-2 retrievals show blowing snow layers averaging ~ 100 m in
379 depth, ranging from ~ 50 m up to 160 m (Fig. 2b). Our previous analysis of ICESat-2
380 observations near the 2019-2020 MOSAiC campaign demonstrated that low level turbulence
often mixes blowing snow to the top of the surface inversion (Robinson et al., 2025), suggesting



381 that blowing snow layer depth may serve as a useful indicator of Arctic inversion depth. Blowing
382 snow optical depths average 0.12 across the Arctic, with maxima near 0.20 in the Fram Strait and
383 southern Baffin Bay. These regions also experience thicker blowing snow layers on average.
384 Figure 2 further shows that regions of deeper, optically thicker blowing snow are co-located with
385 areas of high occurrence frequency and stronger winds.
386



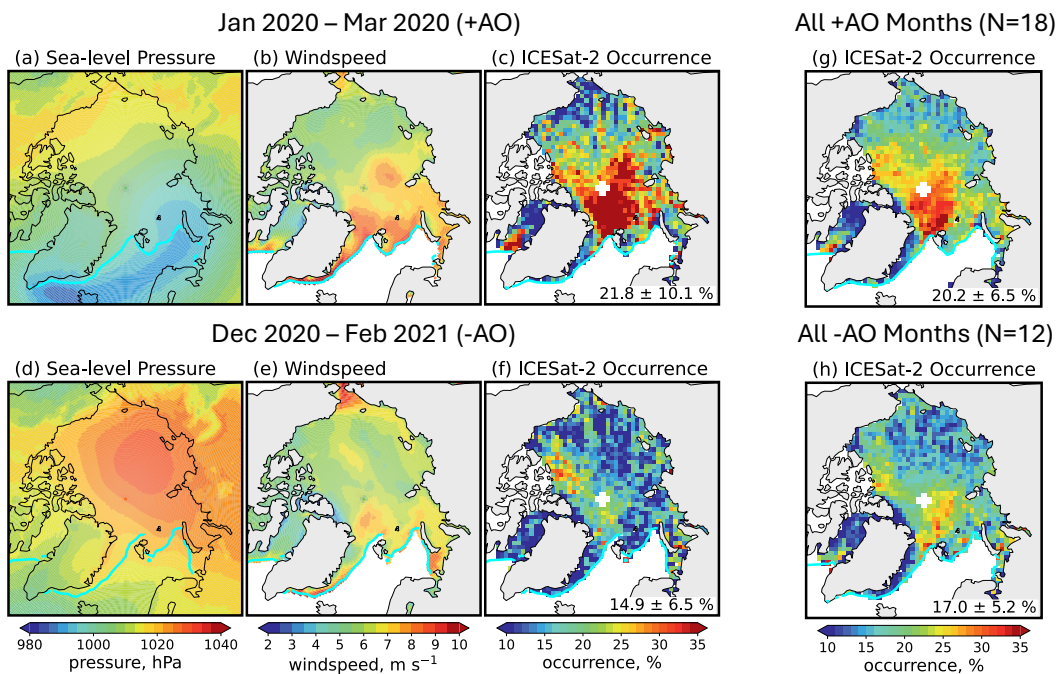
387
388
389 **Figure 3.** Interannual spatial variability of blowing snow occurrence frequency (units %) from ICESat-2
390 observations during the 2018-2023 cold seasons. Each panel shows the average pan-Arctic occurrence and standard
391 deviation (lower right). The cyan line marks the 15% sea ice concentration contour.
392

393 Figure 3 shows that the ICESat-2 pan-Arctic blowing snow occurrence frequencies are consistent
394 from year-to-year at 18-20%. The spatial pattern of occurrence also remains fairly consistent,
395 with the Central Arctic and Fram Strait displaying the highest frequencies and only moderate
396 shifts in location. Despite this, the Central Arctic can display substantial year-to-year variability.
397 For example, the highest (2019-2020) and lowest (2020-2021) pan-Arctic frequencies were
398 observed in consecutive cold seasons.
399

400 The contrast between these two cold seasons appears closely aligned with large scale climate and
401 atmospheric circulation patterns, particularly the Beaufort High and the Arctic Oscillation (AO).
402 In early 2020, a record positive AO phase (+3.5, top row Fig. S3) coincided with a collapse of
403 the Beaufort High, enhanced cyclone activity (Ballinger et al., 2021; Rinke et al., 2021), and
404 widespread blowing snow. From January to March 2020, MERRA-2 sea-level pressure (SLP)
405 and windspeed featured an elongated region of consistently low pressure (< 1,000 hPa) extending
406 from Iceland into the ice-covered Kara and Barents Seas (Fig. 4a). Over these regions and the
407 Central Arctic, mean windspeeds reached 7-9 m s⁻¹ (Fig. 4b). During this period, ICESat-2
408 observed several intense blowing snow episodes covering more than 25% of sea ice area
409 (blowing snow > 1 × 10⁶ km²; Fig. S4), with mean pan-Arctic blowing snow frequencies of
410 21.9%, reaching up to 50% in the Central Arctic (Fig. 4c).



411



412

413

414 **Figure 4.** Comparison of (a,d) MERRA-2 sea-level pressure (hPa), (b,e) MERRA-2 wind speed (m s⁻¹), and (b,d)
 415 ICESat-2 observed blowing snow occurrence frequency (%) for January 2020 – March 2020 (a-c) and December
 416 2020 – February 2021 (d-f). (g,h) Composite ICESat-2 blowing snow occurrence frequency for months with (g)
 417 positive and (h) negative Arctic Oscillation phases during the 2018-2023 cold seasons.

418

419 In contrast, the 2020-2021 season was marked by a strong negative AO (-2.4, top row Fig. S3)
 420 and a persistent Beaufort High (mean MERRA-2 SLP > 1,020 hPa across most of the Arctic
 421 basin, Fig. 4d), conditions known to suppress storm activity (Kenigson & Timmermans, 2021;
 422 Serreze & Barrett, 2011). Consistent with this pattern, MERRA-2 windspeeds were on average ~
 423 2 m s⁻¹ lower relative to January-March 2020 (Fig. 4e). From December 2020 to February 2021
 424 ICESat-2 detected substantially less blowing snow (47% lower relative to Jan-Mar 2020), with
 425 frequencies in the Central Arctic maximizing at only ~ 25% (Fig. 4f). Across all months, we find
 426 a moderately strong correlation between AO phase and ICESat-2 blowing snow occurrence ($r =$
 427 0.62; Fig. S3c). Composites highlight this relationship: positive AO months (N=18; Fig. 4g)
 428 exhibit 20% more blowing snow than negative AO months (N=12, Fig. 4h), with particularly
 429 large differences (up to a factor of two) in the Fram Strait and Central Arctic.

430

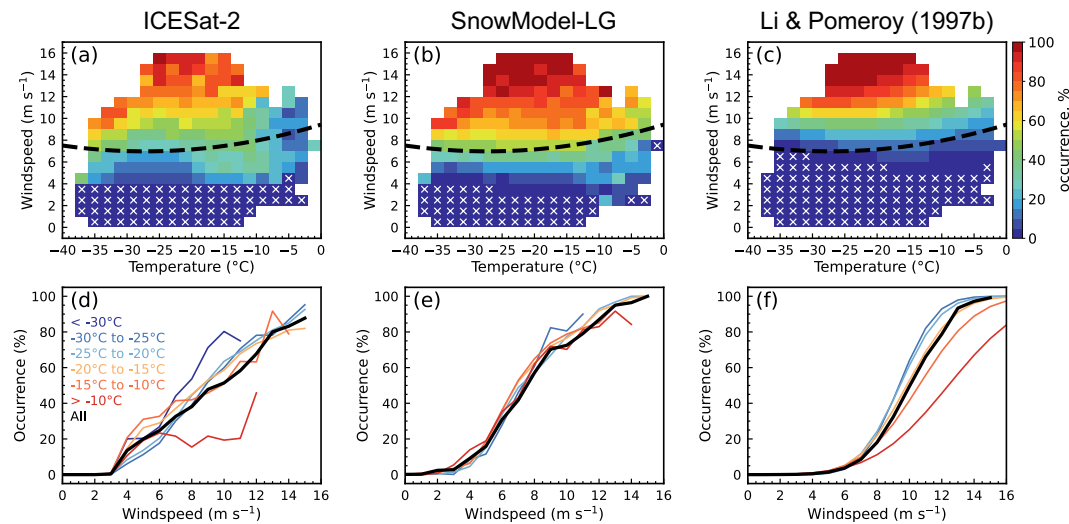
431 3.2 Relationship between windspeed and blowing snow

432

433 In the following section we focus on the Central Arctic region during January-March, the region
 434 most well-sampled by ICESat-2 and months least affected by optically thick clouds (Fig. S2). To
 435 examine relationships between meteorological factors and blowing snow, we use daily 100 km
 436 grid-cell averages. Although this lowers the total number of samples compared to a profile-based
 437 approach, averaging helps to reduce noise.



438



439

440

441 **Figure 5.** Top row: Dependence of blowing snow occurrence frequency on windspeed and temperature for (a)
 442 ICESat-2, (b) SnowModel-LG (blowing snow transport fluxes $> 0.20 \text{ Mg m}^{-2} \text{ d}^{-1}$), and (c) Li & Pomeroy (1997b)
 443 (mean snow age = 72 hours). White stippling represents conditions with no blowing snow; the black dashed line
 444 shows the DY2001 threshold windspeed. Bottom row: Dependence of blowing snow occurrence frequency on
 445 windspeed for all temperatures (black), and for different temperature ranges ($< -30^\circ\text{C}$; -30° to -25°C ; -20° to -15°C ;
 446 -15° to -10°C ; $> -10^\circ\text{C}$) for (d) ICESat-2, (e) SnowModel-LG, and (f) Li & Pomeroy (1997b).

447

448

449 Figure 5 compares the blowing snow occurrence as a function of windspeed and temperature.
 450 For comparison to ICESat-2 and SnowModel-LG, the blowing snow occurrence from Li &
 451 Pomeroy (1997b) is also shown (see their Eq. 7). The blowing snow occurrence from Li &
 452 Pomeroy (1997b) is based on a statistical analysis of observations for 16 stations on the prairies
 453 of western Canada and is a function of windspeed, temperature, and snow age (assumed in our
 454 analysis to be 72 hours). It is also in contrast to DY2001, where the threshold windspeed
 455 essentially acts as an on-off switch for blowing snow. ICESat-2 retrievals indicate a 10-40%
 456 blowing snow occurrence below the DY2001 threshold of $\sim 7 \text{ m s}^{-1}$ (black dashed line, Fig. 5a),
 457 with a much stronger dependence on windspeed than on temperature (Fig. 5a). For example, at 8 m s^{-1} ,
 458 the ICESat-2 occurrence is 50-60 % across all temperatures, while at -25°C it rises from
 459 10-15% at 4 m s^{-1} to $> 80 \text{ %}$ at 15 m s^{-1} . SnowModel-LG predictions (defined as blowing snow
 460 transport $> 0.20 \text{ Mg m}^{-2} \text{ d}^{-1}$) display frequencies $\sim 10 \text{ %}$ larger than ICESat-2 on average but
 461 capture similar features (Fig. 5b). The occurrence of blowing snow predicted from Li & Pomeroy
 462 (1997b) displays a narrower transition region, increasing sharply from $< 20 \text{ %}$ to $> 60 \text{ %}$ over the
 463 $8-10 \text{ m s}^{-1}$ range.

464

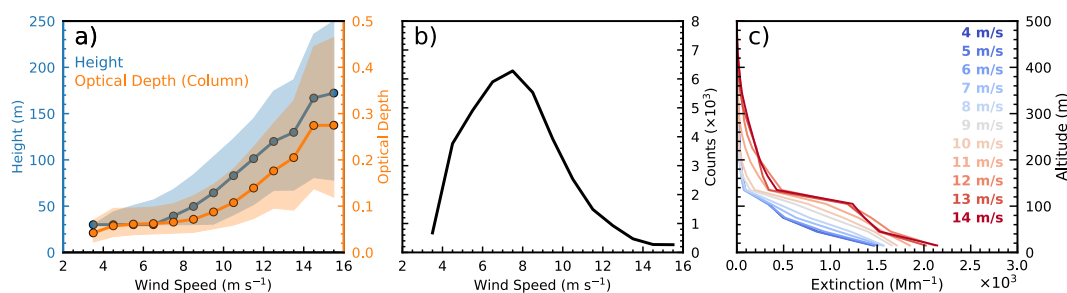
465 The one-dimensional distributions (Fig. 5d-f) further emphasize the dominant control of
 466 windspeed, with all three datasets showing increasing occurrence with stronger winds. ICESat-2
 467 and SnowModel-LG show a weak temperature dependence, with slightly lower occurrence at
 468 higher temperatures, especially for stronger winds, consistent with enhanced snow cohesion and
 469 bonding resistance (Fig. 5d,e). The Li & Pomeroy (1997b) formulation shows a stronger
 temperature sensitivity, ranging from 75% at $T < -30^\circ\text{C}$ to 20% at $T > -5^\circ\text{C}$ for a 10 m s^{-1}



470 windspeed (Fig. 5e). The temperature dependence is likely stronger because of our assumption of
471 a fixed snow age of 72 hours. Snow age also influences bonding and cohesion, with older snow
472 being more resistant to erosion. Because SnowModel-LG and ICESat-2 sample a range of snow
473 ages, their apparent temperature dependence is likely weaker.

474

475 ICESat-2 blowing snow properties also show a strong dependence on windspeed (Fig. 6a).
476 Median blowing snow layer height increases from 30 m at windspeeds of $\sim 4 \text{ m s}^{-1}$ to more than
477 150 m at windspeeds $> 14 \text{ m s}^{-1}$. Optical depth exhibits a similar relationship, rising from 0.02 to
478 0.26 over the same windspeed range. The spread in both height and optical depth (shading, Fig.
479 6a) also widens with increasing windspeed, which we attribute to increased noise from fewer
480 observations in the highest windspeed bins (Fig. 6b).
481



482

483

484 **Figure 6.** Dependence of ICESat-2 blowing snow height and optical depth on windspeed. (a) Median (circles with
485 line) and interquartile range (shading) of ICESat-2 retrieved blowing snow geometric depth (blue) and optical depth
486 (orange) as a function of 10 m windspeed, using 0.5 m s^{-1} bins. (b) Number of grid cells (in thousands) in each
487 windspeed bin from panel a. (c) Mean blowing snow extinction profiles from ICESat-2 retrievals in February 2022
488 ($N = 678,914$), grouped in 1 m s^{-1} wide windspeed bins.

489

490 The increase in blowing snow optical depth reflects a combination of increased blowing snow
491 height and stronger backscatter signal (Fig. 5c). Across nearly 700,000 ICESat-2 retrievals in
492 February 2022, near-surface blowing snow extinction increased by 40% from $1.5 \times 10^3 \text{ Mm}^{-1}$ at 4 m s^{-1} to $2.1 \times 10^3 \text{ Mm}^{-1}$ at 14 m s^{-1} . The enhancement is even larger aloft (a factor of 2-3).
493 Together, these results indicate that stronger winds loft more blowing snow higher into the
494 atmosphere, consistent with previous studies (Palm et al., 2011, 2018; Robinson et al., 2025).
495

496

497 4 Contribution of blowing snow to the Arctic snow-on-sea ice budget

498

499 In this section we examine the contribution of blowing snow to the Arctic cold season snow-on-
500 sea-ice budget. We focus on column integrated blowing snow mass transport (Q , in Eq. 1) and
501 sublimation (Q_{bs} in Eq. 1) fluxes, placing them in the context of one another and comparing them
502 to accumulated snowfall. When interpreting the magnitude of the ICESat-2 estimates, we note
503 that they depend on assumptions inherent to the backscatter-to-flux conversions (Palm et al.,
504 2017; Robinson et al., 2025), including prescribed blowing snow particle sizes and the use of
505 modeled meteorological fields to represent near-surface windspeed, temperature, and humidity
506 (section 2.1). Blowing snow particle sizes are assumed to decrease exponentially with height,
507 while sublimation rates increase with higher temperatures and lower humidities.

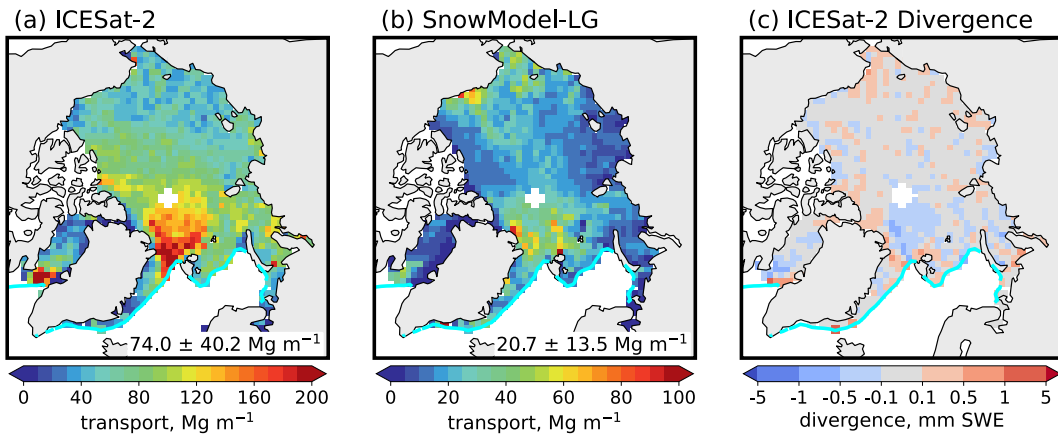
508



509 **4.1 Blowing snow transport from ICESat-2 and SnowModel-LG**

510

511 Figure 7 shows the spatial distribution of blowing snow transport flux inferred from ICESat-2.
512 The flux is calculated by combining the ICESat-2 derived mass concentrations with the vertical
513 profile of windspeed, integrated over the depth of the blowing snow layer. The pan-Arctic mean
514 transport flux observed by ICESat-2 is 74 Mg m^{-1} , with maxima $> 160 \text{ Mg m}^{-1}$ in the Central
515 Arctic, co-located with regions of frequent and intense blowing snow (Fig. 1). SnowModel-LG
516 produces a similar spatial distribution but yields transport fluxes that are 2-3 times lower. This
517 discrepancy likely arises because SnowModel-LG confines blowing snow to the lowest several
518 meters of the atmosphere, where winds are weaker. In contrast, ICESat-2 detects blowing snow
519 layers extending several hundred meters above the surface (Fig. 1b, 6a), where stronger winds
520 enhance snow transport. To support this interpretation, we examined the pan-Arctic blowing
521 snow burdens (mass per square meter; Fig. S5) and found that they agree to within about 20%
522 between ICESat-2 (0.17 g m^{-2}) and SnowModel-LG (0.14 g m^{-2}). In the Central Arctic regions of
523 enhanced transport, both datasets have mean blowing snow burdens of up to 0.40 g m^{-2} .
524



525

526

527 **Figure 7.** Mean 2018-2023 cold season blowing snow transport flux (Mg m^{-1}) from (a) ICESat-2 and (b)
528 SnowModel-LG. Note the color scale for SnowModel-LG is different than for ICESat-2. (c) Divergence of blowing
529 snow transport inferred from ICESat-2 (mm SWE).

530

531 Although the spatial pattern of transport broadly agrees, our seasonal values are smaller than
532 those reported by J. Yang et al. (2010). Their simulations for December 2006 – February 2007
533 suggested transport fluxes up to 800 Mg m^{-1} in the Central Arctic and $> 1,000 \text{ Mg m}^{-1}$ along
534 Greenland's east coast. These higher values could reflect methodological differences: their
535 model did not explicitly account for variable snowpack conditions, which could lead to an
536 overestimate in blowing snow occurrence and transport, and was run at finer spatial (18 km) and
537 temporal (5 s) resolutions, which could capture small-scale wind gradients and localized
538 enhancements in snow redistribution. Despite these differences, both our results and those of J.
539 Yang et al. (2010) indicate that blowing snow transport plays a relatively minor role in the basin-
540 scale snow budget. For example, the divergence of ICESat-2 transport (Fig. 7e) is limited to a
541 few tenths of mm SWE, with localized maxima near 1 mm SWE in regions of frequent blowing
542 snow.



543

544 4.2 Multi-year estimates of blowing snow sublimation

545

546 Figure 8 shows the mean total annual blowing snow sublimation and snowfall for the 2018-2023
547 cold seasons. Pan-Arctic blowing snow sublimation totals from ICESat-2 (1.63 cm SWE) are in
548 close agreement with SnowModel-LG (1.66 cm SWE) and within 30% of DY2001 (2.07 cm
549 SWE). All three estimates are broadly consistent with previous modeling studies (Chung et al.,
550 2011; Liston et al., 2020; J. Yang et al., 2010). In the Central Arctic near Svalbard, ICESat-2
551 indicates the highest values of sublimation (3-4 cm SWE). A secondary maximum (> 3 cm SWE)
552 occurs in the Barents Sea, where blowing snow is retrieved half as often. This reflects the
553 sensitivity of sublimation to temperature and humidity, because the marginal seas are generally
554 warmer than the Central Arctic (Fig. S6). Thus, the reduced occurrence of blowing snow is offset
555 by higher temperatures and lower humidity, which enhance sublimation.

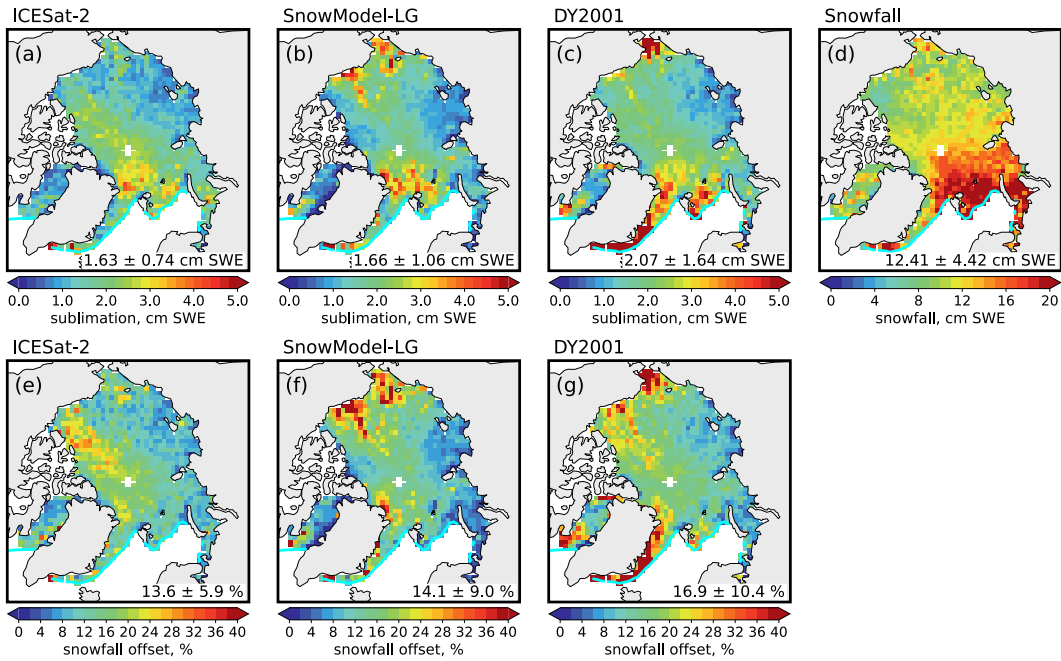
556

557 We compare blowing snow sublimation to total MERRA-2 snowfall over the cold season (12.41
558 cm SWE, Fig. 8d). On average, we find that blowing snow removes 13.6% (ICESat-2), 14.1%
559 (SnowModel-LG), and 16.9% (DY2001) of snowfall. The regional impact, however, varies
560 strongly (Fig.s 8e-g). In the Kara and Barents Seas, where snowfall is highest, sublimation
561 removes only 5-10% of snowfall. In the Central Arctic losses increase to 18-24%, while in
562 regions with more moderate snowfall, such as the Beaufort Sea, sublimation losses can exceed
563 30% (e.g., 2-3 cm SWE of sublimation compared to 8-10 cm SWE of snowfall).

564

565 The fraction of snowfall removed by blowing snow sublimation inferred from ICESat-2 reaches
566 30% in the Beaufort Sea north of the Canadian Arctic Archipelago (Fig. 8e). SnowModel-LG
567 and DY2001 show a similar enhanced offset, though their maxima are shifted southeastward
568 along the coast of Alaska (Fig. 8f,g). The 2018-2023 period was marked by several strong
569 Beaufort High episodes, such as the 2021-22 event highlighted in Fig. 4 (NSIDC, 2021), which
570 are typically associated with calm, dry conditions. Under such conditions, ICESat-2 retrievals
571 may occasionally overestimate blowing snow. False positives could arise when low-level ice
572 crystals (ice clouds or diamond dust) mix with blowing snow, leading the entire ICESat-2
573 backscatter signal to be misattributed to blowing snow. This effect was most pronounced during
574 winter 2021-2022, when exceptionally warm ($T > -20^{\circ}\text{C}$) and dry ($\text{RH}_{\text{ice}} < 90\%$) conditions
575 prevailed north of the Canadian Arctic Archipelago (Fig. S7).

576



577
 578

579 **Figure 8.** Spatial distribution of blowing snow sublimation, total snowfall, and the contribution of blowing snow
 580 sublimation to snowfall offset over Arctic sea ice during 2018-2023. (a-c) Total blowing snow sublimation (cm
 581 SWE) inferred from (a) ICESat-2, (b) SnowModel-LG, and (c) DY2001. (d) Total MERRA-2 snowfall (cm SWE).
 582 (e-g) Percent of snowfall removed by blowing snow sublimation ($= 100 \times [\text{sublimation} / \text{snowfall}]$) from (e) ICESat-2,
 583 (f) SnowModel-LG, and (g) DY2001.

584

585 Along Greenland's east coast, DY2001 predicts much higher sublimation fluxes ($4-5$ cm SWE, $>$
 586 70% of snowfall) than either ICESat-2 and SnowModel-LG ($2-3$ cm SWE, 20-30% of snowfall).
 587 This discrepancy likely reflects DY2001's simple threshold-based parameterization, which tends
 588 to overpredict blowing snow at the typical windspeeds in this region ($6-8$ m s $^{-1}$, Fig. 1). Warmer
 589 and drier conditions in this region (Fig. S6) further amplify the sublimation predicted by
 590 DY2001.

591

592 Daily pan-Arctic time series (Fig. 9) show that blowing snow sublimation is nearly continuous
 593 throughout the cold season, punctuated by sharp peaks during major storm events. The most
 594 intense episodes (> 0.04 cm SWE d $^{-1}$ averaged over sea ice) occur only a few times per season
 595 and correspond to widespread blowing snow detected by ICESat-2 (Fig. S4). These storms
 596 contribute disproportionately to the seasonal total, with individual events removing up to 60% of
 597 daily snowfall (Fig. S7). Between storms, sublimation persists at lower but steady rates ($0.01-$
 598 0.02 cm SWE d $^{-1}$) and these background losses accumulate to a substantial share (35-40%) of the
 599 seasonal total.

600



601
 602
 603
 604
 605
 606
 607

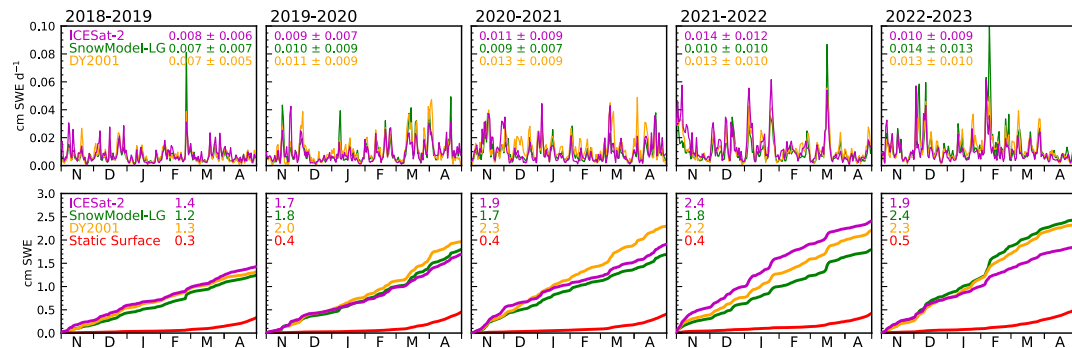


Figure 9. Timeseries of blowing snow sublimation across five Arctic cold seasons. **(top row)** Daily blowing snow sublimation (cm SWE d⁻¹) inferred from ICESat-2 (magenta line) and predicted by SnowModel-LG (green line) and DY2001 (orange line). **(bottom row)** Cumulative daily blowing snow sublimation (cm SWE). The red lines in the bottom row represent the cumulative static surface (non-blown snow) sublimation predicted by SnowModel-LG.

608
 609
 610
 611
 612
 613
 614
 615
 616
 617
 618
 The ICESat-2 inferred sublimation ranges from 1.4 to 2.4 cm SWE across the five cold seasons (Fig. 9, bottom row), corresponding to a 11–20% offset of seasonal snowfall. Both snowfall and blowing snow sublimation vary by 1–2 cm SWE year to year, but the two do not always covary. For example, the 2021–2022 cold season had the lowest snowfall (11.9 cm SWE) yet the highest ICESat-2 sublimation (2.4 cm SWE, 20% offset). Conversely, 2018–2019 featured higher snowfall (12.9 cm SWE) but relatively low sublimation (1.4 cm SWE, 11% offset). These interannual differences highlight that sublimation depends not only on storm frequency and strength (which also drive snowfall) but also on atmospheric conditions which regulate blowing snow occurrence and sublimation efficiency. SnowModel-LG and DY2001 generally agree with the ICESat-2 sublimation, though DY2001 tends to predict slightly higher values.

619
 620
 621
 622
 623
 624
 625
 626
 627
 628
 Blowing snow sublimation exceeds surface sublimation by a factor of 4–5, underscoring the dominant role of blowing snow in sublimation-driven snow loss during much of the cold season. The cumulative surface sublimation timeseries (Q_{ss} in Eq. 1) predicted by SnowModel-LG is shown in Fig. 9 (red lines, bottom row). Seasonal total surface sublimation averages only 0.3–0.5 cm SWE, with nearly all of it occurring from late February through April, when solar radiation increases, near-surface air warms, and RH_{ice} decreases. These values are lower than the 1–2 cm SWE reported by Déry and Yau (2002), likely because their annual means included the warmer spring and summer months. Consistent with this, SnowModel-LG calculates an Arctic-wide annual mean surface sublimation of ~1 cm SWE.

629
 630
 631
 632
 633
 634
 635
 636
 637
 ICESat-2 likely underestimates blowing snow sublimation because it cannot observe blowing snow beneath optically thick clouds. These conditions are most frequent during winter storms, when strong winds can drive intense sublimation. To assess this sampling bias, we examine the 2018–2023 SnowModel-LG and DY2001 predictions under all conditions (i.e., regardless of whether ICESat-2 detected the surface). The all-conditions maps (Fig. S9) show patterns similar to Fig. 8 but with magnitudes 16–25% larger. Pan-Arctic blowing snow sublimation totals increase to 2.1 cm SWE for SnowModel-LG and 2.4 cm SWE for DY2001. Comparing these values to the seasonal snowfall from Fig. 8 (12.4 cm SWE) yields offsets of 17% for SnowModel-LG and 19% for DY2001. This comparison suggests that ICESat-2 captures the



638 spatial pattern and temporal variability of blowing snow sublimation well but underestimates the
639 total by roughly 20% due to this sampling bias.

640

641 **5 Summary and conclusions**

642

643 We presented the first multi-year pan-Arctic estimates of blowing snow derived from ICESat-2
644 satellite observations, extending our earlier single-year analysis (Robinson et al., 2025) to five
645 cold seasons (November through April, 2018-2023). ICESat-2 retrievals allowed us to
646 characterize blowing snow occurrence and properties (geometric and optical depths), and, when
647 combined with assumptions about particle sizes and meteorology from reanalysis, to infer
648 blowing snow sublimation and evaluate its contribution to the Arctic snow-on-sea ice budget.

649

650 Over the five seasons analyzed, ICESat-2 retrievals indicate a mean pan-Arctic blowing snow
651 occurrence of 19%, with maxima exceeding 30% in the Central Arctic and Atlantic sector,
652 regions frequently impacted by storms arriving from lower latitudes. Retrieved blowing snow
653 geometric and optical depths also maximize in these regions. Interannual variability of blowing
654 snow occurrence is substantial and is driven by the Arctic Oscillation (AO). We find that positive
655 AO periods have lower SLP and higher winds, and ~ 50% more blowing snow than negative AO
656 periods. In the Central Arctic, blowing snow occurrence during the positive AO phase was more
657 than twice that of the negative phase, a pattern consistent across all five seasons.

658

659 ICESat-2 observations confirm that windspeed is the primary driver of blowing snow
660 occurrence, with temperature acting as a secondary modulating factor. Blowing snow occurrence
661 increases with windspeed across all temperatures, exceeding 80% at 12 m s^{-1} . The physics-based
662 threshold windspeed in SnowModel-LG (4.5 m s^{-1}) is 2.3 m s^{-1} lower than in DY2001 ($\sim 7 \text{ m s}^{-1}$)
663 and aligns more closely with the windspeeds at which ICESat-2 reliably detects blowing snow.
664 Both ICESat-2 and SnowModel-LG suggest blowing snow occurrence frequencies of 10-40% at
665 windspeeds $4-7 \text{ m s}^{-1}$, where DY2001 predicts no blowing snow. Windspeed also strongly
666 controls blowing snow height and optical depth: blowing snow heights increase from 30 m at 4 m s^{-1}
667 to almost 200 m at 15 m s^{-1} , while optical depths rise from 0.02 to 0.26 over the same
668 range, driven by enhanced backscatter over deeper heights.

669

670 Maximum mass transport fluxes peak where blowing snow is most frequent, with seasonal means
671 of 74 Mg m^{-1} for ICESat-2 and 21 Mg m^{-1} for SnowModel-LG. This factor of three difference
672 reflects SnowModel-LG's confinement of blowing snow to the lowest few meters, where winds
673 are weaker, while ICESat-2 detects layers extending to several hundreds of meters, where
674 stronger winds drive greater transport. Yet, pan-Arctic burdens agree within ~20% (0.17 g m^{-2}
675 for ICESat-2 vs. 0.14 g m^{-2} for SnowModel-LG), underscoring that while the vertical extent is
676 different, the overall mass is consistent. Despite high transport, divergence in ICESat-2 inferred
677 mass flux contributes minimally to the snow budget (maximum of 1 mm SWE).

678

679 We find that blowing snow sublimation plays an important role in the Arctic snow-on-sea-ice
680 budget, reaching up to 5 cm SWE in the Central Arctic, and averaging 1.63-2.07 cm SWE over
681 all sea ice. This is equivalent to a 13.6-16.9% removal of seasonal snowfall on average, with as
682 much as 30% removal in some regions such as the Beaufort Sea. The pan-Arctic ICESat-2
683 inferred blowing snow sublimation ranged from 1.4 to 2.4 cm SWE (11-20% snowfall offset)



684 across the five cold seasons, with similar estimates from SnowModel-LG (1.2-2.4 cm SWE) and
685 DY2001 (1.3-2.3 cm SWE). SnowModel-LG and DY2001 predictions under all conditions (i.e.,
686 including those without ICESat-2 observations due to sampling or clouds) suggest pan-Arctic
687 blowing snow sublimation could be ~20% larger (2.1-2.4 cm SWE) than was found using
688 ICESat-2, resulting in a larger snowfall removal of 17-19%. SnowModel-LG indicates that
689 sublimation from blowing snow is up to a factor of five larger than surface sublimation, which
690 offsets only an additional 2-4% of snowfall.
691

692 Our analysis is limited by a number of factors, including the sampling pattern of ICESat-2.
693 While the high resolution of atmospheric backscatter allows unprecedented detail into blowing
694 snow, the narrow spatial sampling requires temporal and spatial averaging, such as binning the
695 ICESat-2 profiles to a 100 km grid, to generate meaningful statistics. This approach improves
696 coverage but smooths fine-scale variability and may underrepresent short-lived or localized
697 blowing snow events. Moreover, the blowing snow algorithm cannot detect blowing snow layers
698 thinner than 20-30 m. Such thin drifting and blowing snow layers are often predicted by
699 SnowModel-LG and DY2001. Nevertheless, these discrepancies in vertical resolution and
700 sampling appear to have a minimal net effect on the overall estimates of blowing snow fluxes,
701 which are similar for all three methods. Our transport and sublimation flux estimates rely on
702 reanalysis meteorology, which has been shown to have biases, particularly at high latitudes (e.g.,
703 Jonassen et al., 2019; Marshall et al., 2018), and currently does not include feedbacks from
704 blowing snow on the temperature and moisture fields. Such feedbacks would tend to suppress
705 sublimation by increasing humidity and cooling the near-surface atmosphere, potentially leading
706 to overestimation of sublimation in our analysis. However, work done on Antarctic blowing
707 snow processes indicates that the entrainment of warmer and drier air present above the blowing
708 snow and surface temperature inversion can reduce or even eliminate this sublimation-humidity
709 feedback (Palm et al., 2018). Incorporating these processes into coupled models would improve
710 the realism of both meteorological forcing and snow-atmosphere interactions.
711

712 Beyond its role in the snow-on-sea-ice budget, blowing snow sublimation also acts as a
713 significant source of moisture and a sink of heat for the atmosphere. The fate of this moisture
714 remains poorly constrained and warrants further study. Blowing snow sublimation over sea ice is
715 also a recognized source of sea salt aerosols (e.g., Frey et al., 2020; Gong et al., 2023; Huang &
716 Jaeglé, 2017; Ranjithkumar et al., 2025). Taken together, these points highlight that blowing
717 snow has the potential to impact a range of polar processes including boundary layer structure,
718 cloud formation and lifetime, atmospheric chemistry, and the surface energy balance. Recent
719 modeling efforts are beginning to account for these processes (e.g., Hofer et al., 2021; Luo et al.,
720 2021), offering new opportunities to improve predictions of Arctic composition, weather, and
721 climate. Such advancements will require robust observational constraints to ensure realism and
722 guide a process-based understanding of the coupled Arctic system. By capturing the vertical and
723 horizontal structure of blowing snow at unprecedented scales, our study demonstrates that
724 spaceborne lidar is a key tool for bridging the gap between observations and models, and for
725 advancing our understanding of the rapidly changing Arctic environment.
726
727
728
729
730



731 **Code and data availability**

732

733 The ICESat-2 ATL09 data used in this study can be accessed through the NASA NSIDC Distributed Active Archive
734 Center (<https://doi.org/10.5067/ATLAS/ATL09.006>). The code and data required to reproduce the figures in this
735 study are available at: <https://doi.org/10.5281/zenodo.18119606>.

736

737 **Author contributions**

738

739 JR and LJ designed the study. SPP aided in ICESat-2 software development and visualization. GEL developed the
740 SnowModel-LG code. JR and LJ performed formal analysis. JR prepared the manuscript with contributions from all
741 co-authors.

742

743 **Competing interests**

744

745 The authors declare that they have no conflict of interest.

746

747 **Acknowledgments**

748

749 The authors express gratitude to the ICESat-2 engineering and science teams for their ongoing efforts to maintain
750 the ATLAS instrument and generate the ICESat-2 atmospheric data products.

751

752 **References**

753

754 Ballinger, T. J., Walsh, J. E., Bhatt, U. S., Bieniek, P. A., Tschudi, M. A., Brettschneider, B., Eicken, H., Mahoney,
755 A. R., Richter-Menge, J., & Shapiro, L. H.: Unusual West Arctic Storm Activity During Winter 2020: Another
756 Collapse of the Beaufort High? *Geophysical Research Letters*, 48(13). <https://doi.org/10.1029/2021gl092518>, 2021.

757 Bintanja, R.: The impact of Arctic warming on increased rainfall. *Scientific Reports*, 8(1), 16001.

758 <https://doi.org/10.1038/s41598-018-34450-3>, 2018.

759 Bintanja, R., & Andry, O.: Towards a rain-dominated Arctic. *Nature Climate Change*, 7(4), 263–267.

760 <https://doi.org/10.1038/nclimate3240>, 2017.

761 Brodzik, M. J., & Knowles, K. W.: Chapter 5: EASE-grid: A versatile set of equal-area projections and grids. In M.
762 F. Goodchild (Ed.), *Discrete global grids: A web book* (pp. 98–113). Santa Barbara, CA: National Center for
763 Geographic Information & Analysis. Retrieved from <https://escholarship.org/uc/item/9492q6sm>, 2002.

764 Chen, W.-N., Chiang, C.-W., & Nee, J.-B.: Lidar ratio and depolarization ratio for cirrus clouds. *Applied Optics*,
765 41(30), 6470. <https://doi.org/10.1364/AO.41.006470>, 2002.

766 Chung, Y.-C., Bélair, S., & Mailhot, J.: Blowing Snow on Arctic Sea Ice: Results from an Improved Sea Ice–Snow–
767 Blowing Snow Coupled System. *Journal of Hydrometeorology*, 12(4), 678–689.

768 <https://doi.org/10.1175/2011JHM1293.1>, 2011.

769 Clancy, R., Bitz, C. M., Blanchard-Wrigglesworth, E., McGraw, M. C., & Cavallo, S. M.: A cyclone-centered
770 perspective on the drivers of asymmetric patterns in the atmosphere and sea ice during Arctic cyclones. *Journal of
771 Climate*, 1–47. <https://doi.org/10.1175/JCLI-D-21-0093.1>, 2022.

772 Dai, A.: Temperature and pressure dependence of the rain-snow phase transition over land and ocean. *Geophysical
773 Research Letters*, 35(12). <https://doi.org/10.1029/2008gl033295>, 2008.

774 Déry, S. J., & Tremblay, L.-B.: Modeling the Effects of Wind Redistribution on the Snow Mass Budget of Polar Sea
775 Ice. *Journal of Physical Oceanography*, 34(1), 258–271. [https://doi.org/10.1175/1520-0485\(2004\)034<0258:MTEOWR>2.0.CO;2](https://doi.org/10.1175/1520-0485(2004)034<0258:MTEOWR>2.0.CO;2), 2004.

777 Déry, S. J., & Yau, M. K.: A Bulk Blowing Snow Model. *Boundary-Layer Meteorology*, 93(2), 237–251.

778 <https://doi.org/10.1023/A:1002065615856>, 1999.

779 Déry, S. J., & Yau, M. K.: Simulation Of Blowing Snow In The Canadian Arctic Using A Double-Moment Model.
780 *Boundary-Layer Meteorology*, 99(2), 297–316. <https://doi.org/10.1023/A:1018965008049>, 2001.



781 Déry, S. J., & Yau, M. K.: Large-scale mass balance effects of blowing snow and surface sublimation. *Journal of*
782 *Geophysical Research: Atmospheres*, 107(D23). <https://doi.org/10.1029/2001JD001251>, 2002.

783 Frey, M. M., Norris, S. J., Brooks, I. M., Anderson, P. S., Nishimura, K., Yang, X., Jones, A. E., Nerentorp
784 Mastromonaco, M. G., Jones, D. H., & Wolff, E. W.: First direct observation of sea salt aerosol production from
785 blowing snow above sea ice. *Atmospheric Chemistry and Physics*, 20(4), 2549–2578. <https://doi.org/10.5194/acp-20-2549-2020>, 2020.

786 Gallée, H., Guyomarc'h, G., & Brun, E.: Impact Of Snow Drift On The Antarctic Ice Sheet Surface Mass Balance:
787 Possible Sensitivity To Snow-Surface Properties. *Boundary-Layer Meteorology*, 99(1), 1–19.
788 <https://doi.org/10.1023/A:1018776422809>, 2001.

789 Gallée, H., Trouvilliez, A., Agosta, C., Genthon, C., Favier, V., & Naaim-Bouvet, F.: Transport of Snow by the
790 Wind: A Comparison Between Observations in Adélie Land, Antarctica, and Simulations Made with the Regional
791 Climate Model MAR. *Boundary-Layer Meteorology*, 146(1), 133–147. <https://doi.org/10.1007/s10546-012-9764-z>,
792 2013.

793 Gelaro, R., McCarty, W., Suárez, M. J., Todling, R., Molod, A., Takacs, L., Randles, C. A., Darmenov, A.,
794 Bosilovich, M. G., Reichle, R., Wargan, K., Coy, L., Cullather, R., Draper, C., Akella, S., Buchard, V., Conaty, A.,
795 da Silva, A. M., Gu, W., ... Zhao, B.: The Modern-Era Retrospective Analysis for Research and Applications,
796 Version 2 (MERRA-2). *Journal of Climate*, 30(14), 5419–5454. <https://doi.org/10.1175/JCLI-D-16-0758.1>, 2017.

797 Gong, X., Zhang, J., Croft, B., Yang, X., Frey, M. M., Bergner, N., Chang, R. Y.-W., Creamean, J. M., Kuang, C.,
798 Martin, R. V., Ranjithkumar, A., Sedlacek, A. J., Uin, J., Willmes, S., Zawadowicz, M. A., Pierce, J. R., Shupe, M.,
799 D., Schmale, J., & Wang, J.: Arctic warming by abundant fine sea salt aerosols from blowing snow. *Nature
800 Geoscience*, 16(9), 768–774. <https://doi.org/10.1038/s41561-023-01254-8>, 2023.

801 Herzfeld, U., Hayes, A., Palm, S., Hancock, D., Vaughan, M., & Barbieri, K.: Detection and Height Measurement of
802 Tenuous Clouds and Blowing Snow in ICESat-2 ATLAS Data. *Geophysical Research Letters*, 48(17),
803 [e2021GL093473](https://doi.org/10.1029/2021GL093473). <https://doi.org/10.1029/2021GL093473>, 2021.

804 Hofer, S., Amory, C., Kittel, C., Carlsen, T., Le Toumelin, L., & Storelvmo, T.: The Contribution of Drifting Snow
805 to Cloud Properties and the Atmospheric Radiative Budget Over Antarctica. *Geophysical Research Letters*, 48(22).
806 <https://doi.org/10.1029/2021gl094967>, 2021.

807 Huang, J., & Jaeglé, L.: Wintertime enhancements of sea salt aerosol in polar regions consistent with a sea ice
808 source from blowing snow. *Atmospheric Chemistry and Physics*, 17(5), 3699–3712. <https://doi.org/10.5194/acp-17-3699-2017>, 2017.

809 Huang, J., Jaeglé, L., Chen, Q., Alexander, B., Sherwen, T., Evans, M. J., Theys, N., & Choi, S.: Evaluating the
810 impact of blowing-snow sea salt aerosol on springtime BrO and O₃ in the Arctic. *Atmospheric Chemistry and Physics*, 20(12), 7335–7358. <https://doi.org/10.5194/acp-20-7335-2020>, 2020.

811 Intrieri, J. M., & Shupe, M. D.: Characteristics and Radiative Effects of Diamond Dust over the Western Arctic
812 Ocean Region. *Journal of Climate*, 17(15), 2953–2960. [https://doi.org/10.1175/1520-0442\(2004\)017<2953:CAREOD>2.0.CO;2](https://doi.org/10.1175/1520-0442(2004)017<2953:CAREOD>2.0.CO;2), 2004.

813 Jonassen, M. O., Välijuso, I., Vihma, T., Uotila, P., Makshtas, A. P., & Launiainen, J.: Assessment of Atmospheric
814 Reanalyses With Independent Observations in the Weddell Sea, the Antarctic. *Journal of Geophysical Research:
815 Atmospheres*, 124(23), 12468–12484. <https://doi.org/10.1029/2019jd030897>, 2019.

816 Josset, D., Pelon, J., Garnier, A., Hu, Y., Vaughan, M., Zhai, P., Kuehn, R., & Lucker, P.: Cirrus optical depth and
817 lidar ratio retrieval from combined CALIPSO-CloudSat observations using ocean surface echo. *Journal of
818 Geophysical Research: Atmospheres*, 117(D5), 2011JD016959. <https://doi.org/10.1029/2011JD016959>, 2012.

819 Kenigson, J. S., & Timmermans, M.-L.: Arctic Cyclone Activity and the Beaufort High. *Journal of Climate*, 34(10),
820 4119–4127. <https://doi.org/10.1175/jcli-d-20-0771.1>, 2021.

821 King, J. C., Anderson, P. S., Vaughan, D. G., Mann, G. W., Mobbs, S. D., & Vosper, S. B.: Wind-borne
822 redistribution of snow across an Antarctic ice rise. *Journal of Geophysical Research: Atmospheres*, 109(D11),
823 [2003JD004361](https://doi.org/10.1029/2003JD004361). <https://doi.org/10.1029/2003JD004361>, 2004.

824



828 Krnavek, L., Simpson, W. R., Carlson, D., Domine, F., Douglas, T. A., & Sturm, M.: The chemical composition of
829 surface snow in the Arctic: Examining marine, terrestrial, and atmospheric influences. *Atmospheric Environment*,
830 50, 349–359. <https://doi.org/10.1016/j.atmosenv.2011.11.033>, 2012.

831 Kwok, R., & Untersteiner, N.: The thinning of Arctic sea ice. *Physics Today*, 64(4), 36–41.
832 <https://doi.org/10.1063/1.3580491>, 2011.

833 Lecomte, O., Fichefet, T., Flocco, D., Schroeder, D., & Vancoppenolle, M.: Interactions between wind-blown snow
834 redistribution and melt ponds in a coupled ocean–sea ice model. *Ocean Modelling*, 87, 67–80.
835 <https://doi.org/10.1016/j.ocemod.2014.12.003>, 2015.

836 Lenaerts, J. T. M., Van Den Broeke, M. R., Déry, S. J., König-Langlo, G., Ettema, J., & Munneke, P. K.: Modelling
837 snowdrift sublimation on an Antarctic ice shelf. *The Cryosphere*, 4(2), 179–190. <https://doi.org/10.5194/tc-4-179-2010>, 2010.

838 Lenaerts, J. T. M., Van Den Broeke, M. R., Van Angelen, J. H., Van Meijgaard, E., & Déry, S. J.: Drifting snow
839 climate of the Greenland ice sheet: A study with a regional climate model. *The Cryosphere*, 6(4), 891–899.
840 <https://doi.org/10.5194/tc-6-891-2012>, 2012.

841 Lesins, G., Bourdages, L., Duck, T. J., Drummond, J. R., Eloranta, E. W., & Walden, V. P.: Large surface radiative
842 forcing from topographic blowing snow residuals measured in the High Arctic at Eureka. *Atmospheric Chemistry
843 and Physics*, 9(6), 1847–1862. <https://doi.org/10.5194/acp-9-1847-2009>, 2009.

844 Li, L., & Pomeroy, J. W. (1997a). Estimates of Threshold Wind Speeds for Snow Transport Using Meteorological
845 Data. *Journal of Applied Meteorology*, 36(3), 205–213. [https://doi.org/10.1175/1520-0450\(1997\)036<0205:EOTWSF>2.0.CO;2](https://doi.org/10.1175/1520-0450(1997)036<0205:EOTWSF>2.0.CO;2)

846 Li, L., & Pomeroy, J. W. (1997b). Probability of occurrence of blowing snow. *Journal of Geophysical Research: Atmospheres*, 102(D18), 21955–21964. <https://doi.org/10.1029/97JD01522>

847 Liston, G. E., & Elder, K.: A Meteorological Distribution System for High-Resolution Terrestrial Modeling
848 (MicroMet). *Journal of Hydrometeorology*, 7(2), 217–234. <https://doi.org/10.1175/jhm486.1>, 2006.

849 Liston, G. E., Haehnel, R. B., Sturm, M., Hiemstra, C. A., Berezovskaya, S., & Tabler, R. D.: Simulating complex
850 snow distributions in windy environments using SnowTran-3D. *Journal of Glaciology*, 53(181), 241–256.
851 <https://doi.org/10.3189/172756507782202865>, 2007.

852 Liston, G. E., Itkin, P., Stroeve, J., Tschudi, M., Stewart, J. S., Pedersen, S. H., Reinking, A. K., & Elder, K.: A
853 Lagrangian Snow-Evolution System for Sea-Ice Applications (SnowModel-LG): Part I—Model Description. *Journal
854 of Geophysical Research: Oceans*, 125(10). <https://doi.org/10.1029/2019JC015913>, 2020.

855 Liston, G. E., Polashenski, C., Rösel, A., Itkin, P., King, J., Merkouriadi, I., & Haapala, J.: A Distributed Snow-
856 Evolution Model for Sea-Ice Applications (SnowModel). *Journal of Geophysical Research: Oceans*, 123(5), 3786–
857 3810. <https://doi.org/10.1002/2017JC013706>, 2018.

858 Liston, G. E., & Sturm, M.: A snow-transport model for complex terrain. *Journal of Glaciology*, 44(148), 498–516.
859 <https://doi.org/10.3189/S0022143000020211>, 1998.

860 Liston, G. E., & Sturm, M.: The role of winter sublimation in the Arctic moisture budget. *Hydrology Research*,
861 35(4–5), 325–334. <https://doi.org/10.2166/nh.2004.0024>, 2004.

862 Luo, L., Zhang, J., Hock, R., & Yao, Y.: Case Study of Blowing Snow Impacts on the Antarctic Peninsula Lower
863 Atmosphere and Surface Simulated With a Snow/Ice Enhanced WRF Model. *Journal of Geophysical Research:
864 Atmospheres*, 126(2). <https://doi.org/10.1029/2020jd033936>, 2021.

864 Mann, G. W., Anderson, P. S., & Mobbs, S. D.: Profile measurements of blowing snow at Halley, Antarctica.
865 *Journal of Geophysical Research: Atmospheres*, 105(D19), 24491–24508. <https://doi.org/10.1029/2000JD900247>,
866 2000.

867 Markus, T., Neumann, T., Martino, A., Abdalati, W., Brunt, K., Csatho, B., Farrell, S., Fricker, H., Gardner, A.,
868 Harding, D., Jasinski, M., Kwok, R., Magruder, L., Lubin, D., Luthcke, S., Morison, J., Nelson, R.,
869 Neuenschwander, A., Palm, S., ... Zwally, J.: The Ice, Cloud, and land Elevation Satellite-2 (ICESat-2): Science
870 requirements, concept, and implementation. *Remote Sensing of Environment*, 190, 260–273.
871 <https://doi.org/10.1016/j.rse.2016.12.029>, 2017.



876 Marshall, G. J., Kivinen, S., Jylhä, K., Vignols, R. M., & Rees, W. G.: The accuracy of climate variability and trends
877 across Arctic Fennoscandia in four reanalyses. *International Journal of Climatology*, 38(10), 3878–3895.
878 <https://doi.org/10.1002/joc.5541>, 2018.

879 McCrystall, M. R., Stroeve, J., Serreze, M., Forbes, B. C., & Screen, J. A.: New climate models reveal faster and
880 larger increases in Arctic precipitation than previously projected. *Nature Communications*, 12(1), 6765.
881 <https://doi.org/10.1038/s41467-021-27031-y>, 2021.

882 Merkouriadi, I., Cheng, B., Graham, R. M., Rösel, A., & Granskog, M. A.: Critical Role of Snow on Sea Ice Growth
883 in the Atlantic Sector of the Arctic Ocean. *Geophysical Research Letters*, 44(20).
884 <https://doi.org/10.1002/2017gl075494>, 2017.

885 Merkouriadi, I., Gallet, J., Graham, R. M., Liston, G. E., Polashenski, C., Rösel, A., & Gerland, S.: Winter snow
886 conditions on Arctic sea ice north of Svalbard during the Norwegian young sea ICE (N-ICE2015) expedition.
887 *Journal of Geophysical Research: Atmospheres*, 122(20). <https://doi.org/10.1002/2017jd026753>, 2017.

888 National Snow and Ice Data Center. (2021, December 2). A mixed-bag of Arctic sea ice. *Sea Ice Today*.
889 <https://nsidc.org/sea-ice-today/analyses/mixed-bag-arctic-sea-ice>

890 Neumann, T. A., Martino, A. J., Markus, T., Bae, S., Bock, M. R., Brenner, A. C., Brunt, K. M., Cavanaugh, J.,
891 Fernandes, S. T., Hancock, D. W., Harbeck, K., Lee, J., Kurtz, N. T., Luers, P. J., Luthcke, S. B., Magruder, L.,
892 Pennington, T. A., Ramos-Izquierdo, L., Rebold, T., ... Thomas, T. C.: The Ice, Cloud, and Land Elevation Satellite
893 – 2 mission: A global geolocated photon product derived from the Advanced Topographic Laser Altimeter System.
894 *Remote Sensing of Environment*, 233, 111325. <https://doi.org/10.1016/j.rse.2019.111325>, 2019.

895 Nishimura, K., & Nemoto, M.: Blowing snow at Mizuho station, Antarctica. *Philosophical Transactions of the
896 Royal Society A: Mathematical, Physical and Engineering Sciences*, 363(1832), 1647–1662.
897 <https://doi.org/10.1098/rsta.2005.1599>, 2005.

898 Palm, S. P., Kayetha, V., & Yang, Y.: Toward a Satellite-Derived Climatology of Blowing Snow Over Antarctica.
899 *Journal of Geophysical Research: Atmospheres*, 123(18). <https://doi.org/10.1029/2018JD028632>, 2018.

900 Palm, S. P., Kayetha, V., Yang, Y., & Pauly, R.: Blowing snow sublimation and transport over Antarctica from 11
901 years of CALIPSO observations. *The Cryosphere*, 11(6), 2555–2569. <https://doi.org/10.5194/tc-11-2555-2017>,
902 2017.

903 Palm, S. P., Y. Yang, U. C. Herzfeld, D. Hancock, K. A. Barbieri, J. Wimert, & the ICESat-2 Science Team.:
904 ATLAS/ICESat-2 L3A Calibrated Backscatter Profiles and Atmospheric Layer Characteristics, Version 6 [Dataset].
905 NASA National Snow and Ice Data Center Distributed Active Archive Center.
906 <https://doi.org/10.5067/ATLAS/ATL09.006>, 2023.

907 Palm, S. P., Yang, Y., Herzfeld, U., Hancock, D., Hayes, A., Selmer, P., Hart, W., & Hlavka, D.: ICESat-2
908 Atmospheric Channel Description, Data Processing and First Results. *Earth and Space Science*, 8(8),
909 e2020EA001470. <https://doi.org/10.1029/2020EA001470>, 2021.

910 Palm, S. P., Yang, Y., Kayetha, V., & Nicolas, J. P.: Insight into the Thermodynamic Structure of Blowing-Snow
911 Layers in Antarctica from Dropsonde and CALIPSO Measurements. *Journal of Applied Meteorology and
912 Climatology*, 57(12), 2733–2748. <https://doi.org/10.1175/JAMC-D-18-0082.1>, 2018.

913 Palm, S. P., Yang, Y., Spinhirne, J. D., & Marshak, A.: Satellite remote sensing of blowing snow properties over
914 Antarctica. *Journal of Geophysical Research*, 116(D16), D16123. <https://doi.org/10.1029/2011JD015828>, 2011.

915 Palm, S. P., Yang, Y., Hertzfeld, U., & Hancock, D.: Ice, Cloud, and Land Elevation Satellite (ICESat-2) Project
916 Algorithm Theoretical Basis Document for the Atmosphere, Part I: Level 2 and 3 Data Products, version 6.
917 <https://doi.org/10.5067/H975R4YYVIT6>, 2022.

918 Pomeroy, J. W., Marsh, P., & Gray, D. M.: Application of a distributed blowing snow model to the Arctic.
919 *Hydrological Processes*, 11(11), 1451–1464. [https://doi.org/10.1002/\(SICI\)1099-1085\(199709\)11:11<1451::AID-HYP449>3.0.CO;2-Q](https://doi.org/10.1002/(SICI)1099-1085(199709)11:11<1451::AID-HYP449>3.0.CO;2-Q), 1997.

920 Ranjithkumar, A., Duncan, E., Yang, X., Partridge, D. G., Lachlan-Cope, T., Gong, X., Nishimura, K., & Frey, M.
921 M.: Direct observation of Arctic Sea salt aerosol production from blowing snow and modeling over a changing sea
922 ice environment. *Elem Sci Anth*, 13(1). <https://doi.org/10.1525/elementa.2024.00006>, 2025.



924 Rantanen, M., Karpechko, A. Yu., Lipponen, A., Nordling, K., Hyvärinen, O., Ruosteenoja, K., Vihma, T., &
925 Laaksonen, A.: The Arctic has warmed nearly four times faster than the globe since 1979. *Communications Earth &*
926 *Environment*, 3(1), 168. <https://doi.org/10.1038/s43247-022-00498-3>, 2022.

927 Rhodes, R. H., Yang, X., Wolff, E. W., McConnell, J. R., & Frey, M. M.: Sea ice as a source of sea salt aerosol to
928 Greenland ice cores: A model-based study. *Atmospheric Chemistry and Physics*, 17(15), 9417–9433.
929 <https://doi.org/10.5194/acp-17-9417-2017>, 2017.

930 Rinke, A., Cassano, J. J., Cassano, E. N., Jaiser, R., & Handorf, D.: Meteorological conditions during the MOSAiC
931 expedition. *Elementa: Science of the Anthropocene*, 9(1), 00023. <https://doi.org/10.1525/elementa.2021.00023>,
932 2021.

933 Robinson, J., Jaeglé, L., Palm, S. P., Shupe, M. D., Liston, G. E., & Frey, M. M.: ICESat-2 observations of blowing
934 snow over Arctic sea ice during the 2019–2020 MOSAiC expedition. *Journal of Geophysical Research: Atmospheres*,
935 130, e2025JD043919. <https://doi.org/10.1029/2025JD043919>, 2025.

936 Schmidt, R. A.: Vertical profiles of wind speed, snow concentration, and humidity in blowing snow. *Boundary-
937 Layer Meteorology*, 23(2), 223–246. <https://doi.org/10.1007/BF00123299>, 1982.

938 Serreze, M. C., & Barrett, A. P.: Characteristics of the Beaufort Sea High. *Journal of Climate*, 24(1), 159–182.
939 <https://doi.org/10.1175/2010jcli3636.1>, 2011.

940 Shupe, M. D., Walden, V. P., Eloranta, E., Uttal, T., Campbell, J. R., Starkweather, S. M., & Shiobara, M.: Clouds
941 at Arctic Atmospheric Observatories. Part I: Occurrence and Macrophysical Properties. *Journal of Applied
942 Meteorology and Climatology*, 50(3), 626–644. <https://doi.org/10.1175/2010JAMC2467.1>, 2011.

943 Stroeve, J., & Notz, D.: Changing state of Arctic sea ice across all seasons. *Environmental Research Letters*, 13(10),
944 103001. <https://doi.org/10.1088/1748-9326/aade56>, 2018.

945 Sturm, M., Holmgren, J., & Perovich, D. K.: Winter snow cover on the sea ice of the Arctic Ocean at the Surface
946 Heat Budget of the Arctic Ocean (SHEBA): Temporal evolution and spatial variability. *Journal of Geophysical
947 Research: Oceans*, 107(C10). <https://doi.org/10.1029/2000jc000400>, 2002.

948 Tschudi, M. A., Meier, W. N., & Stewart, J. S.: An enhancement to sea ice motion and age products at the National
949 Snow and Ice Data Center (NSIDC). *The Cryosphere*, 14(5), 1519–1536. <https://doi.org/10.5194/tc-14-1519-2020>,
950 2020.

951 Tschudi, M. & Univ Of CO.: Polar Pathfinder Daily 25 km EASE-Grid Sea Ice Motion Vectors [Dataset]. NASA
952 National Snow and Ice Data Center Distributed Active Archive Center. <https://doi.org/10.5067/INAWUWO7QH7B>,
953 2019.

954 Valkonen, E., Cassano, J., & Cassano, E.: Arctic Cyclones and Their Interactions With the Declining Sea Ice: A
955 Recent Climatology. *Journal of Geophysical Research: Atmospheres*, 126(12).
956 <https://doi.org/10.1029/2020jd034366>, 2021.

957 Webster, M., Gerland, S., Holland, M., Hunke, E., Kwok, R., Lecomte, O., Massom, R., Perovich, D., & Sturm, M.:
958 Snow in the changing sea-ice systems. *Nature Climate Change*, 8(11), 946–953. [https://doi.org/10.1038/s41558-018-0286-7](https://doi.org/10.1038/s41558-018-
959 0286-7), 2018.

960 Winker, D. M., Vaughan, M. A., Omar, A., Hu, Y., Powell, K. A., Liu, Z., Hunt, W. H., & Young, S. A.: Overview
961 of the CALIPSO Mission and CALIOP Data Processing Algorithms. *Journal of Atmospheric and Oceanic
962 Technology*, 26(11), 2310–2323. <https://doi.org/10.1175/2009JTECHA1281.1>, 2009.

963 Yang, J., & Yau, M. K.: A New Triple-Moment Blowing Snow Model. *Boundary-Layer Meteorology*, 126(1), 137–
964 155. <https://doi.org/10.1007/s10546-007-9215-4>, 2007.

965 Yang, J., Yau, M. K., Fang, X., & Pomeroy, J. W.: A triple-moment blowing snow-atmospheric model and its
966 application in computing the seasonal wintertime snow mass budget. *Hydrology and Earth System Sciences*, 14(6),
967 1063–1079. <https://doi.org/10.5194/hess-14-1063-2010>, 2010.

968 Yang, X., Frey, M. M., Rhodes, R. H., Norris, S. J., Brooks, I. M., Anderson, P. S., Nishimura, K., Jones, A. E., &
969 Wolff, E. W.: Sea salt aerosol production via sublimating wind-blown saline snow particles over sea ice:
970 Parameterizations and relevant microphysical mechanisms. *Atmospheric Chemistry and Physics*, 19(13), 8407–
971 8424. <https://doi.org/10.5194/acp-19-8407-2019>, 2019.



972 Yang, X., Pyle, J. A., & Cox, R. A.: Sea salt aerosol production and bromine release: Role of snow on sea ice.
973 *Geophysical Research Letters*, 35(16), L16815. <https://doi.org/10.1029/2008GL034536>, 2008.
974 Yang, Y., Palm, S. P., Marshak, A., Wu, D. L., Yu, H., & Fu, Q.: First satellite-detected perturbations of outgoing
975 longwave radiation associated with blowing snow events over Antarctica. *Geophysical Research Letters*, 41(2),
976 730–735. <https://doi.org/10.1002/2013GL058932>, 2014.
977 Zhang, D., Vogelmann, A., Kollias, P., Luke, E., Yang, F., Lubin, D., & Wang, Z.: Comparison of Antarctic and
978 Arctic Single-Layer Stratiform Mixed-Phase Cloud Properties Using Ground-Based Remote Sensing Measurements.
979 *Journal of Geophysical Research: Atmospheres*, 124(17–18), 10186–10204. <https://doi.org/10.1029/2019JD030673>,
980 2019.